Hydrodynamical Particle Containment in a Rotor-Stator Spinning Disk Device

Kevin M. P. van Eeten, Dennis H. J. Hülsman, John van der Schaaf, and Jaap C. Schouten
Laboratory of Chemical Reactor Engineering, Dept. of Chemical Engineering and Chemistry,
Eindhoven University of Technology, 5600 MB Eindhoven, The Netherlands

DOI 10.1002/aic.14886
Published online June 5, 2015 in Wiley Online Library (wileyonlinelibrary.com)

A novel type of rotor-stator spinning disk device is proposed which allows for the entrapment of solid particles solely by hydrodynamic means. In this new configuration, the solid rotating disk is replaced with two conjoined rotors with a variable gap spacing. Liquid is fed through the top stator and can flow out again through the rotor-rotor interior and the hollow rotation axis. Moreover, the volume between the two rotors is optionally filled with a highly porous reticulated carbon foam. It was found that particle containment was strongly improved by the presence of this reticulated foam as it hinders the buildup of centripetal boundary layer flow near the disks in the interior of the rotor-rotor assembly. These centripetal boundary layers drag along particles resulting in a loss of containment. Experiments utilizing glass beads showed that particles with a diameter down to 17.8 μm can be completely entrapped when a carbon foam is placed between the two conjoined disks at rotor speeds up to the maximum investigated value of 178 rad s^{-1}. Additionally, the rotor-rotor gap did not have an effect on the particle entrapment level when the reticulated carbon foam was omitted and can be ascribed to the build-up of boundary layers, which is independent of rotor-rotor distance. *AIChE J*, 61: 3656–3665, 2015
Keywords: rotor-stator spinning disk reactor, hydrodynamical particle containment, boundary layer flow

Introduction

The rotor-stator spinning disk reactor is a novel type of chemical reactor which shows excellent heat- and mass-transfer performance, opening up intensified windows of operation for multiphase and/or highly exothermic processes as sulphonation, halogenation, or nitrification. The basics of the reactor, schematically depicted in Figure 1, typically consists of a rapidly rotating solid disk (the rotor) encased by a narrow cylindrical housing (the stator). The high rotational velocities of the rotor of up to $\Omega_{max}=2000$ rpm, combined with the very small rotor-stator spacing of one to several millimeters, lies at the heart of the reactor's mass-transfer performance.[1]

The high velocity gradients in the fluids present between the rotor and the stator lead to high shear forces on droplets or bubbles being formed, triggering early pinch-off from their inlet points.[2] These smaller bubbles and droplets then give rise to an increase in the interfacial area, a, available for molecular transport. The high degree of turbulence invoked by the high rotational velocity of the disk allows for the rapid renewal of fluid elements near the surfaces of bubbles, droplets, and particles, lowering the resistance to mass transfer and leading to an increase in the mass-transfer coefficient, k. It is the combination of these two effects that makes the rotor-stator spinning disk reactor such a versatile multiphase chemical reactor.

Correspondence concerning this article should be addressed to J. C Schouten at J.C.Schouten@tue.nl.

For the case of gas-liquid mass transfer, a study by Meeuwse et al.[3] has shown that the gas-liquid mass-transfer rate can be as high as $k_{GL}a_{GL}=0.95\,m_L^3\,m_R^{-3}\,s^{-1}$, which is about four times higher than typical values in bubble columns and twice as high as values in a traditional thin film spinning disk reactor.[4,5] Furthermore, when the relatively low gas hold-up ($\varepsilon_G=0.021\,m_G^3\,m_R^{-3}$) is taken into account, values of the gas-liquid mass transfer rate per unit volume of gas are calculated to be $k_{GL}a_{GL}/\varepsilon_G=20.5\,m_L^3\,m_G^{-3}\,s^{-1}$, which are about 40 times higher than reported values for more traditional reactors.[6]

When considering solid-liquid mass transfer, values up to $k_{LS}a_{LS}=0.25\,m_L^3\,m_R^{-3}\,s^{-1}$ were reported by Meeuwse et al.[7] In that investigation, the rotating disk was catalytically coated with platinum on a Nafion-coating so as to effectively contain the catalytic solids inside the reactor. Although depositing and immobilizing catalyst on the disk might indeed prevent the necessity of downstream separation of the solid fraction, it does limit the mass-transfer rate as both the interfacial area and the mass-transfer coefficient are lowered by this configuration. One would preferably be able to freely suspend, leading to a high k_{LS}-value, catalytic particles with a small diameter, and thus a high a_{LS}-value, without allowing them to exit the system together with the outgoing stream.

This article presents a new configuration of the rotor-stator spinning disk reactor with a rotor-rotor assembly filled with a highly porous reticulated carbon foam. This novel device will be shown to achieve such complete particle entrapment without the use of mechanical filters, or downstream processing of the effluent stream. The article is structured as follows: first,

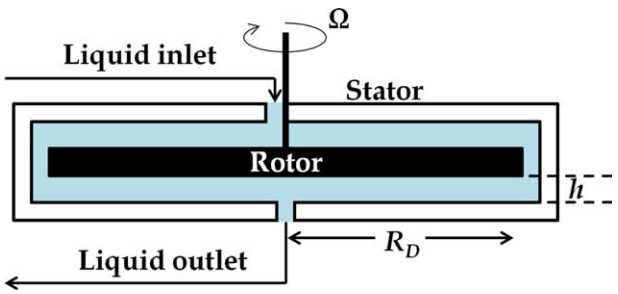

Figure 1. The rotor-stator spinning disk reactor consists of a rapidly rotating disk (the rotor) with angular velocities up to Ω_{max}=2000 rpm.

The rotor is enclosed by a narrow cylindrical housing (the stator), where the rotor-stator spacing, *h*, is of the order of one to several millimeters. [Color figure can be viewed in the online issue, which is available at wileyonlinelibrary.com.]

the hydrodynamics of rotor-stator, and rotor-rotor flow is discussed from which the general operating principle of the reactor can be explained. This is then followed by a description of the experimental setup and the experimental method to test particle containment. Subsequently, the image analysis method is discussed which was used to analyze the microscopic photographs that where made during the experiments. After that, the experimental results are discussed and interpreted, and the article finishes with some concluding remarks.

Hydrodynamics and Working Principle

The working principle of the novel rotor-stator spinning disk device can be explained via Figure 2. Similar to the more conventional rotor-stator spinning disk reactor, the setup consists of a rotating part inside a stationary shroud. Liquid is fed near the axis of rotation through the top stator [part (1) in Figure 1] and leaves through the hollow axis of rotation, part (2) in Figure 1. The rotating part in this configuration does not consist of a single solid disk, but comprises a construction of two parallel conjoined disks through which liquid can flow radially inward toward the hollow axis and out of the reactor.

The two distinct liquid regions between the two conjoined rotating disks (3), or between the rotor and the stator (4), both serve a different purpose with regard to the operating principle of the reactor. The liquid flow between the rotating and stationary disks (4) enhances the distribution and recirculation of solid particles inside of the reactor, while simultaneously increasing mass-transfer rates. The rotor-rotor flow field (3) on the other hand prevents solid particles from leaving the reactor. Both effects are caused by hydrodynamical properties of the flow field, and can be understood by considering the fluid dynamics near rotating and stationary disks.

The hydrodynamics near rotating disks have been intensively studied as it was the first geometrical configuration which could potentially lead to a full analytic solution of the Navier–Stokes equations. For the case of an infinitely extended fluid over an infinite rotating disk, Von Kármán[8] showed that the set of partial differential equations describing fluid motion can be simplified to a system of ordinary differential equations with a so-called Von Kármán similarity transformation. This mathematical transform follows from the assumption that the velocity normal to the disk is a function of the distance from the disk only.

Numerical solutions of these ordinary differential equations showed that all velocity gradients were confined to a boundary layer near the rotating disk termed the Von Kármán boundary layer.[8,9] Within this boundary layer, the azimuthal velocity decreases to zero while moving axially away from the disk. There is furthermore a radial outflow invoked by the centrifugal motion of the disk, which is balanced by continuity with an axial flow toward the disk.

The reverse situation was studied by Bödewadt,[10] where an infinitely extended rotating fluid flows over an infinite stationary disk. By again applying the same similarity transformation with a different set of boundary conditions, it was found that the velocity gradients were confined to a Bödewadt boundary layer attached to the stationary disk. In this layer, the azimuthal velocity gradually decreases to zero when approaching the disk. The centrifugal motion of the fluid in this boundary layer led to a pressure increase when moving radially away from the axis of rotation resulting in a centripetal flow of fluid within this boundary layer. By continuity, this radial inflow is then balanced by an axial flow away from the disk.

Batchelor[11] proved that Von Kármán's similarity hypothesis could also be applied to flow situations between two parallel disks, one rotating and one stationary. According to Batchelor, the flow field would consist of a Von Kármán boundary layer near the rotor, a Bödewadt boundary layer near the stator, separated by a core region of constant azimuthal velocity, and zero radial velocity.

The existence of this core region in inviscid flow was later challenged by Stewartson.[12] Following the same similarity

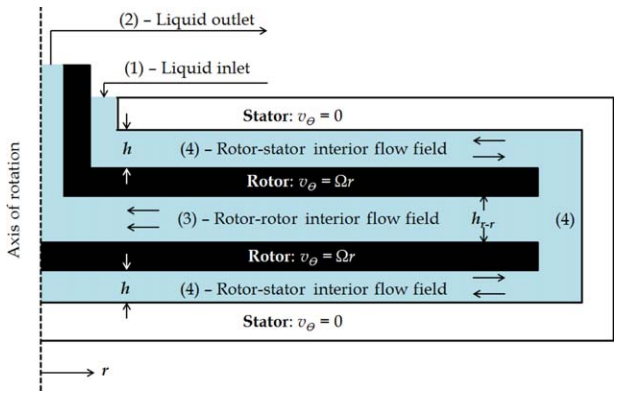

Figure 2. Particles with a higher density than the liquid are entrapped in this setup due to an increased centrifugal force in the rotor-rotor interior flow field.

Liquid is fed through the top stator at position (1), and leaves through the hollow axis at (2). There are two distinct liquid regions with different hydrodynamics inside the setup: a rotor-rotor region (3), and a rotor-stator region (4). In the rotor-stator flow field, there is a net centrifugal outflow from the liquid inlet toward the edge of the disk while the azimuthal velocity lies somewhere in between the velocity of the rotor and zero, that is, the velocity of the stator. The fluid flow inside the rotor-rotor assembly is centripetal in nature and has a higher azimuthal velocity than the one between the rotor and the stator. This increased centrifugal force will effectively cause containment of solid particles which have a higher density than the liquid. [Color figure can be viewed in the online issue, which is available at wileyonlinelibrary.com.]

transformation, Stewartson argued that both the Bödewadt boundary layer and the region of inviscid rotation do not exist and apart from the Von Kármán boundary layer near the rotor, the majority of the fluid would be at rest. These seemingly incompatible views lead to decades of discussion on the existence and uniqueness of either of the solutions until it was later shown that, in fact, Batchelor's and Stewartson's results were both solutions of the ODEs (Ordinary Differential Equations) following the Von Kármán similarity transformation.[13] In fact, a whole range of solutions was found to exist depending on the Reynolds number.[14]

The specific flow field in the rotor-stator region of any spinning disk setup can be identified by the definitions given by Daily and Nece[15] which was further delineated in a flow map by Djaoui et al.[16] Depending on the Reynolds number and the gap ratio, four different flow regimes were observed. Regime I is observed at low Reynolds numbers and small gap spacings. In this case, the liquid flow field consists of a Von Kármán boundary layer near the rotor in direct contact with a Bödewadt boundary layer. As the gap spacing increases at a constant Reynolds number, the two boundary layers get separated by a core region in inviscid, rotational motion in Regime II. Regimes III and IV are then the turbulent analogons of Regimes I and II, respectively.

As this novel rotor-stator spinning disk device is operated at high angular velocities and small disk spacings, the flow field inside the rotor-stator regime, (4) in Figure 2, is of the type characterized by Regime III. There exists therefore a high amount of shear in the region between the rotor and the stator, increasing mass transfer. Simultaneously, the large boundary layer flows guarantee a more uniform spatial distribution of solid particles inside the reactor.

The flow field in the interior domain between the two rotating disks, (3) in Figure 2, shows a somewhat different behavior compared to the rotor-stator flow. As there is a net throughflow, ϕ_v, between the rotating disks, there are two effects of the radial position on the intrinsic fluid dynamics. One part of the flow field will be proportional to the angular velocity of the disk which scales linearly with r as $v_{\text{rotation}} \propto \Omega r$, while the part that scales with the net flow is reciprocal to r according to $v_{\text{flow}} \propto \phi_v / 2\pi r h$. Obviously, centripetal flow will induce a drag force on a particle, dragging it radially inward, while the centrifugal field will force particles radially outward when particles are more dense than the surrounding liquid. At the outer edge of the disk, fluid flow will be dominated by rotation instead of throughflow, so any solid particle heavier than water will experience a net centrifugal force. Moreover, as centrifugal buoyancy scales with particle volume and centripetal drag with particle surface, depending on the size of the particle, the presented spinning disk assembly will fully contain solid particles, while simultaneously freely suspending them.

This somewhat over-simplified situation is disturbed, however, by a secondary effect described by Owen and Pincombe[17] and Owen et al.[18]. Angular momentum, a conserved quantity, is transported radially inward between the two conjoined rotors. As the radial distance to the axis of rotation decreases for inflowing fluid elements, by conservation of angular momentum, the azimuthal velocity of the liquid increases, leading to a situation where the liquid in the interior between the conjoined rotors have a higher angular velocity than the disks. Similar to the situation described by Bödewadt[10] where a rotating fluid near a stationary disk invokes a Bödewadt type of boundary layer, two centripetal boundary layer flows are formed near the rotors focusing the net throughflow in these narrow layers. The drag force on particles between the conjoined rotors subsequently strongly increases as v_{flow} is no longer reciprocal to the rotor-rotor spacing, but to the much smaller boundary layer thickness. Moreover, as this boundary layer thickness is proportional to $\Omega_{\text{core}}^{-\frac{1}{2}}$,[19] increasing the angular velocity of the disk will, counterintuitively, lead to a poorer entrapment of solid particles in the reactor. Additionally, and contrary to the case of rotor-stator flow, the boundary layer thickness is independent of the distance between the disks, so that an increasing h_{r-r} will not reduce the drag force experienced by the particles.

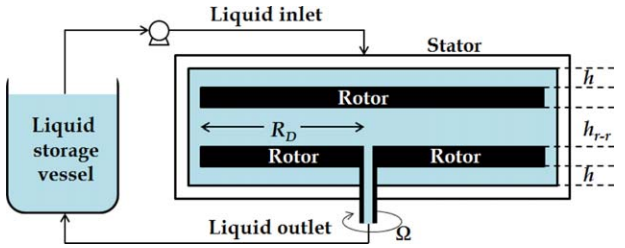

Figure 3. The experimental setup consists of a modified rotor-stator spinning disk assembly with a PMMA housing and two conjoined anodized aluminum rotors.

The rotor-stator spacing is equal to $h = 1$ mm, while the rotor radius equals $R_D = 6.6$ cm. The rotor-rotor interdisk spacing can be set to either $h_{r-r} = 1$ mm, or $h_{r-r} = 10$ mm. Moreover, for the case where $h_{r-r} = 10$ mm, a reticulated carbon foam block can be placed between the two conjoined rotating disks. [Color figure can be viewed in the online issue, which is available at wileyonlinelibrary.com.]

Obviously, placing a mechanical filter between the two rotors will prevent particles from leaving the reactor, but at the cost of a very high pressure drop when entrapping very small particles. This can be prevented by placing a highly porous solid foam between the two rotating disks which acts as a hydrodynamical filter instead of a mechanical one. Because the foam is highly porous, liquid will suffer negligible additional pressure drop when flowing radially inward between the rotors, but the foam will hinder the build-up of the undesired boundary layer flow.

Based on these hydrodynamical considerations, this novel rotor-stator spinning disk configuration can be divided into two distinct zones which both influence the reactor operation in their own way. The rotor-stator flow consists of a centrifugal von Kármán boundary layer at the rotor in close contact with a centripetal Bödewadt boundary layer near the stator, introducing a recirculation increasing homogeneity in the spatial distribution of solid particles. At the same time, the high degree of shear in this narrow region between the rotor and the stator increases solid liquid mass transfer by rapidly replacing fluid elements at the particle surfaces. The rotor-rotor region on the other hand, when the centripetal boundary layer flow can be negated, hydrodynamically entraps solid particles without introducing high pressure drops normally occurring over mechanical filters.

Experimental Setup and Procedure

A schematic representation of the experimental setup is shown in Figure 3. The setup consists of a PMMA (poly methyl metacrylate) housing encasing a set of two anodized aluminum disks. The spacing between the housing and the rotor was fixed

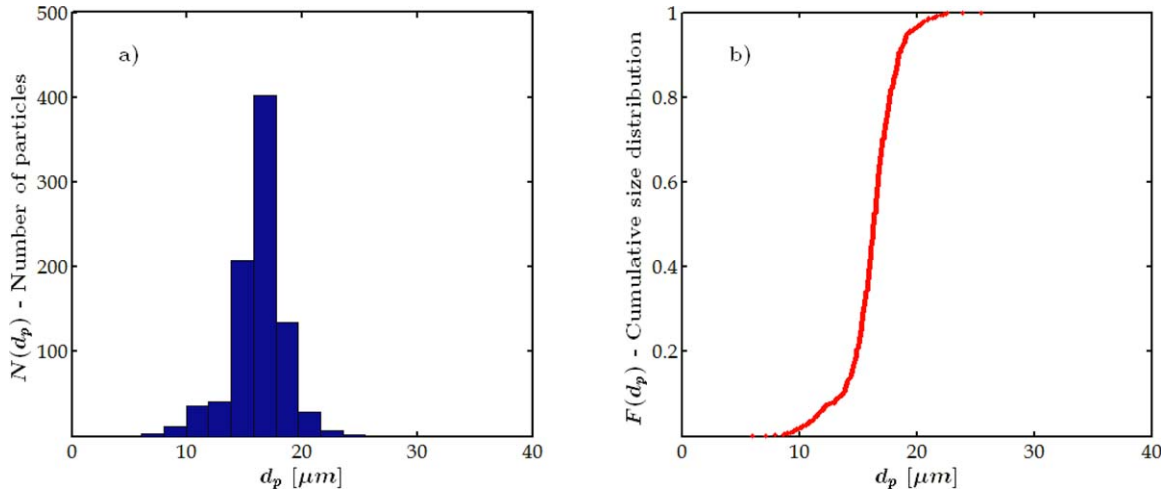

Figure 4. Particle-size distribution of 1–30 μm spherical glass beads as supplied by Polysciences prod. nr. 07668.

In panel (a) a bar plot is shown, while panel (b) depicts the cumulative particle-size distribution. [Color figure can be viewed in the online issue, which is available at wileyonlinelibrary.com.]

at $h = 1$ mm, the rotor radius was given by $R_D = 6.6$ cm, while the rotor-rotor distance could be varied with the help of spacers to values of $h_{r-r} = 1$ mm, or $h_{r-r} = 10$ mm. When $h_{r-r} = 10$ mm, the rotor-rotor interior domain can accommodate the presence of a 20 PPI Duocel Reticulated Vitreous Carbon foam disk with a radius of 5.7 mm and height of 1 cm. The foam was kept in place by the spacers used to tune h_{r-r}. The carbon foam had a 3% nominal density of the bulk material and a specific area of 1066 $m^2\ m^{-3}$.

Particle entrapment was tested for three cases:

- A rotor-rotor distance of $h_{r-r} = 1$ mm, without reticulated foam.
- A rotor-rotor distance of $h_{r-r} = 10$ mm, without reticulated foam.
- A rotor-rotor distance of $h_{r-r} = 10$ mm, with reticulated foam.

To test the maximum size of particles that could be entrapped, spherical glass beads were used. Three particle-size distributions were investigated: Polysciences prod. nr. 07668, 189201, and 15926. The particle-size distributions were determined using the method discussed in Section Image Analysis. The results of these analyses are given in Figures 4–6, respectively.

Note that the 20 PPI carbon foam has a pore diameter of 1.27 mm, which is one to two orders of magnitudes larger than the diameter of the glass beads, effectively ruling out the effect of mechanical filtering on the results.

For every experiment, first an amount of 0.25 g of intermediately sized glass beads (30–50 μm) and 0.25 g of larger glass beads (50–100 μm) with particle-size distributions as in Figures 5 and 6, respectively, were weighed on a Sartorius LE623S and subsequently suspended in 250 mL of demineralized water. The disk rotational velocity was set to its maximum value of $\Omega = 178$ rad s^{-1}, after which the suspension was fed to the reactor at a flow rate of 4.39 mL s^{-1} using a Masterflex 7523-35 peristaltic pump with a 77200-60 easy-load II head. The aqueous suspension was fed to the system through the stator, exited via the hollow rotor through the

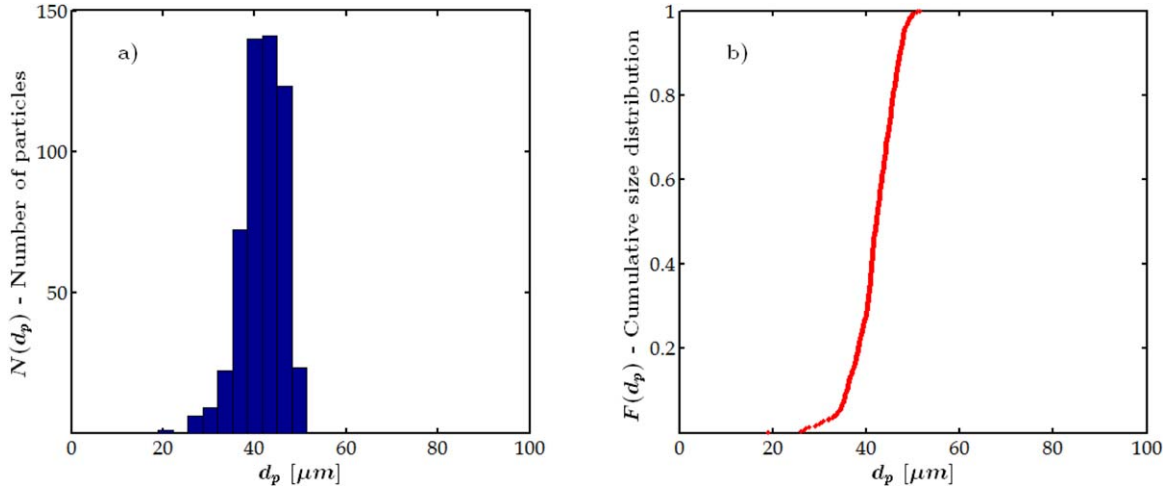

Figure 5. Particle-size distribution of 30–50 μm spherical glass beads as supplied by Polysciences prod. nr. 189201.

In panel (a) a bar plot is shown, while panel (b) depicts the cumulative particle-size distribution. [Color figure can be viewed in the online issue, which is available at wileyonlinelibrary.com.]

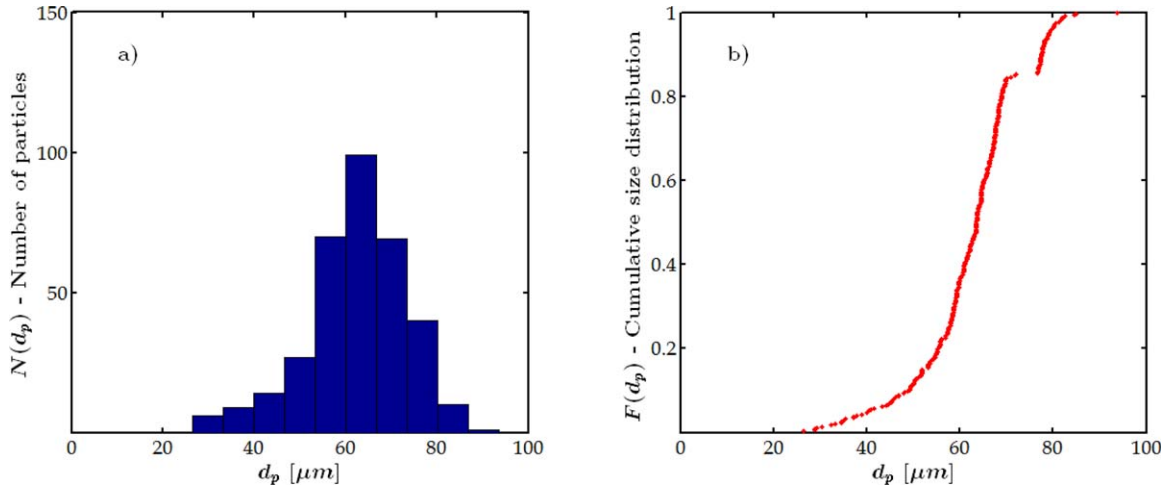

Figure 6. Particle-size distribution of 50–100 μm spherical glass beads as supplied by Polysciences prod. nr. 15926.

In panel (a) a bar plot is shown, while panel (b) depicts the cumulative particle-size distribution. Notice that the jump in the cumulative particle-size distribution in panel (b) around 70–80 μm suggests a mixture of two different particle size fractions. [Color figure can be viewed in the online issue, which is available at wileyonlinelibrary.com.]

rotational shaft, and recycled to the liquid storage vessel. At this highest rotational velocity, the centrifugal forces on the glass beads are highest, potentially leading to maximum achievable particle containment.

At each rotational velocity, a minimum of four samples were taken with a Pasteur pipette. Several milliliters of suspension were extracted from the liquid vessel and deposited on a Petri dish. This process was repeated after each

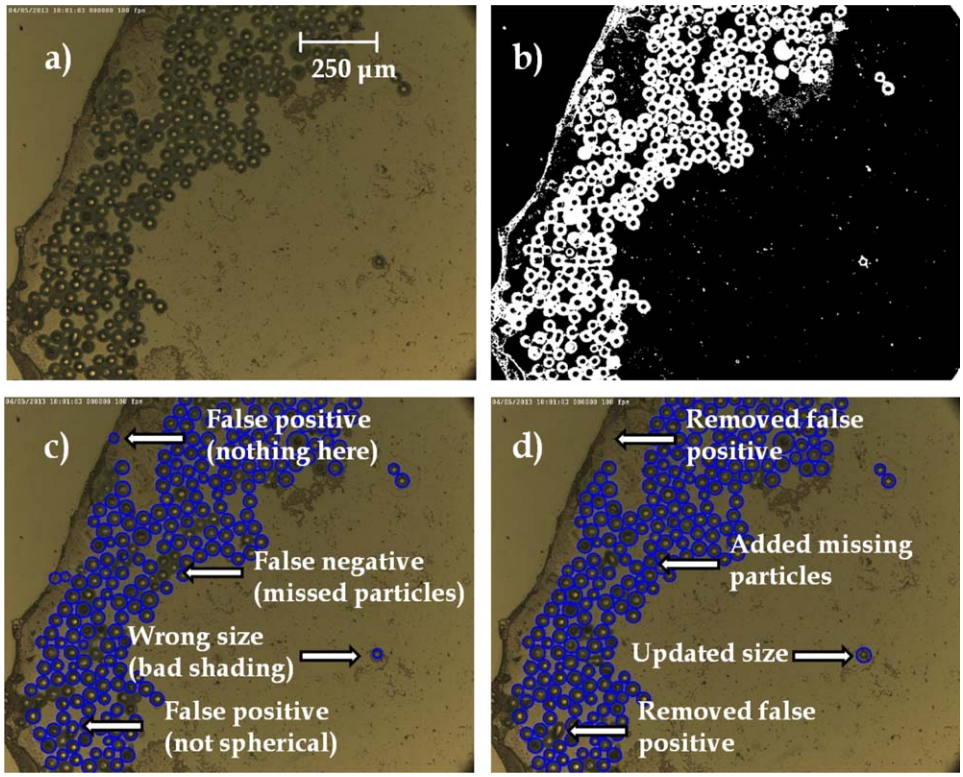

Figure 7. The image analysis process can be detailed in this example photograph taken from a sample corresponding to experimental conditions where no foam filler was used, $h_{r-r} = 1$ mm, and the rotational velocity of the rotor was set to 52.4 rad s^{-1}.

The original image in panel (a) was first converted to a black and white picture in (b) in such a way that the balance between true positives and false positives was optimal. Moreover, by carefully tuning the threshold factor between black and white and the sensitivity factor for the Phase Coding method in `imfindcircles`, the circular fit over the particle edges could be optimized, in a way that the fitted circle did not overlap the particle shadow, or lay within the particle interior. The circles that were then found by `imfindcircles` after this first analysis can be seen in panel (c), after which false positives were removed, missed particles were added, and the sensitivity factor and threshold level were locally enhanced to account for gradients in background lighting. The final result of detected particles and diameters are given in panel (d). [Color figure can be viewed in the online issue, which is available at wileyonlinelibrary.com.]

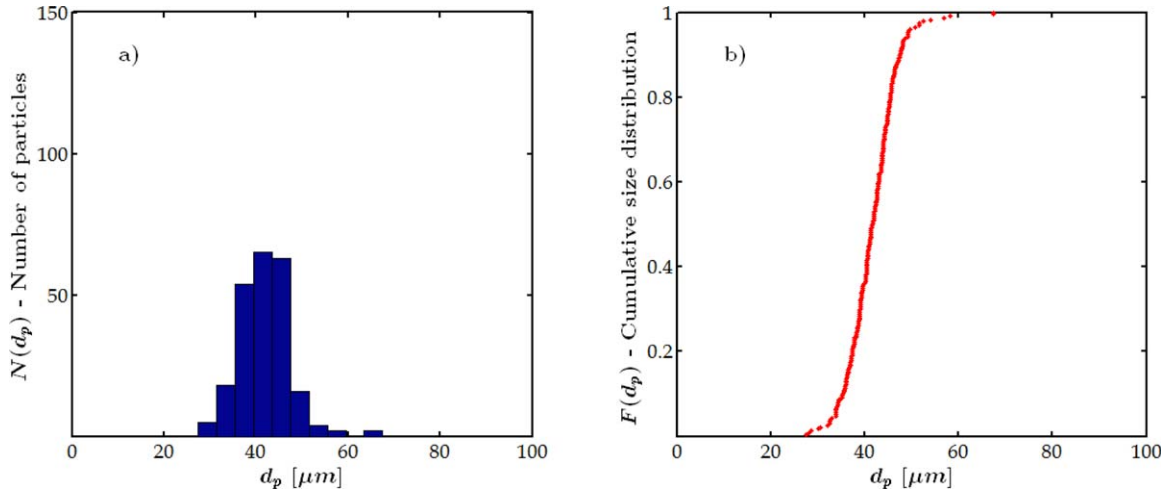

Figure 8. Panel (a) shows a bar plot of the experimental result corresponding to Figure 7, while panel (b) details the corresponding cumulative particle-size distribution.

After analyzing all photographs corresponding to an experimental run, the average particle diameter, standard deviation, maximum observed particle diameter, and the 99% confidence interval were determined for further analysis. [Color figure can be viewed in the online issue, which is available at wileyonlinelibrary.com.]

incremental decrease of the rotational velocity of the disk. Each Petri dish was dried overnight in an oven at 80°C after which microscopic photographs were taken on an Zeiss Axio Observer D1m microscope and an IDT Motionpro X3plus camera. The entire Petri dish was carefully inspected visually through the microscope so that the photographs that were taken were as representative of the whole sample as possible. Whenever it was found that the intermediate and large glass beads were fully entrapped inside the experimental setup, the experiment was repeated with 0.5 g of 1–30 μm particles to determine the lower limit of particle diameters that could be entrapped.

Between series of consecutive experiments, the carbon foam remained in place. The foam was regenerated by flushing the entire setup with distilled water while the rotor-rotor assembly was alternatingly kept stationary, or at low spinning speed. The effluent stream was collected until no more particles were present in this stream and was discarded along with the suspension in the storage vessel. After the experiments, the setup was opened and the reticulated carbon foam was removed. The setup and the foam were subsequently flushed with demineralized water. The particles that were collected in the washing water were discarded along with the suspension in the feed vessel.

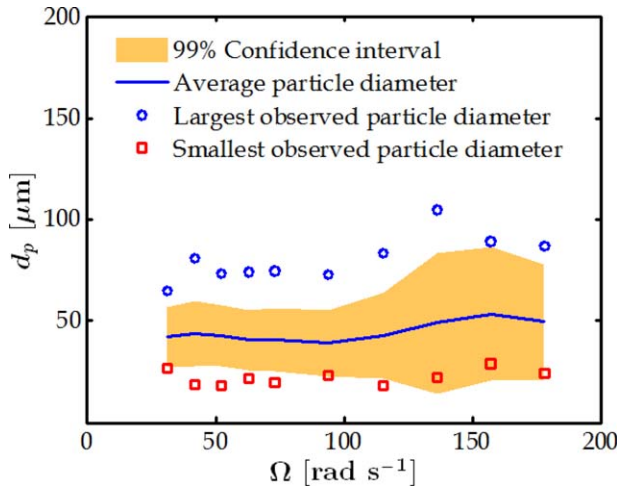

Figure 9. The containment of glass beads is poor for the experiments where the rotor-rotor spacing was set to 1 mm without using a reticulated carbon foam.

The formation of Bödewadt boundary layers which act as a focusing region for the net throughflow results in higher centripetal drag forces resulting in poor entrapment results. [Color figure can be viewed in the online issue, which is available at wileyonlinelibrary.com.]

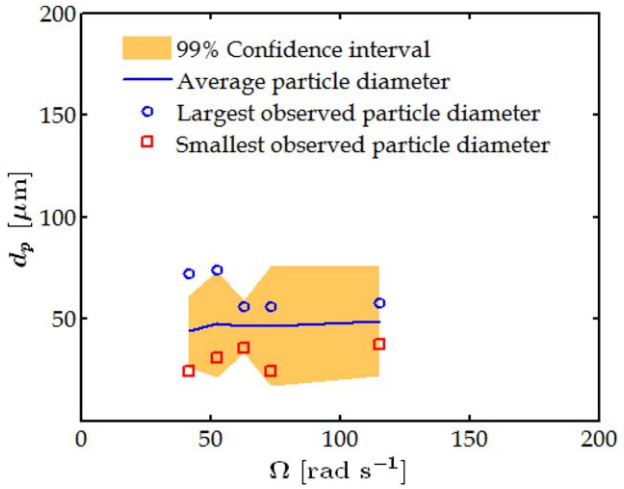

Figure 10. The containment of glass beads is poor for the experiments where the rotor-rotor spacing was set to 10 mm without using a reticulated carbon foam.

The formation of Bödewadt boundary layers which act as a focusing region for the net throughflow results in higher centripetal drag forces resulting in poor entrapment results. [Color figure can be viewed in the online issue, which is available at wileyonlinelibrary.com.]

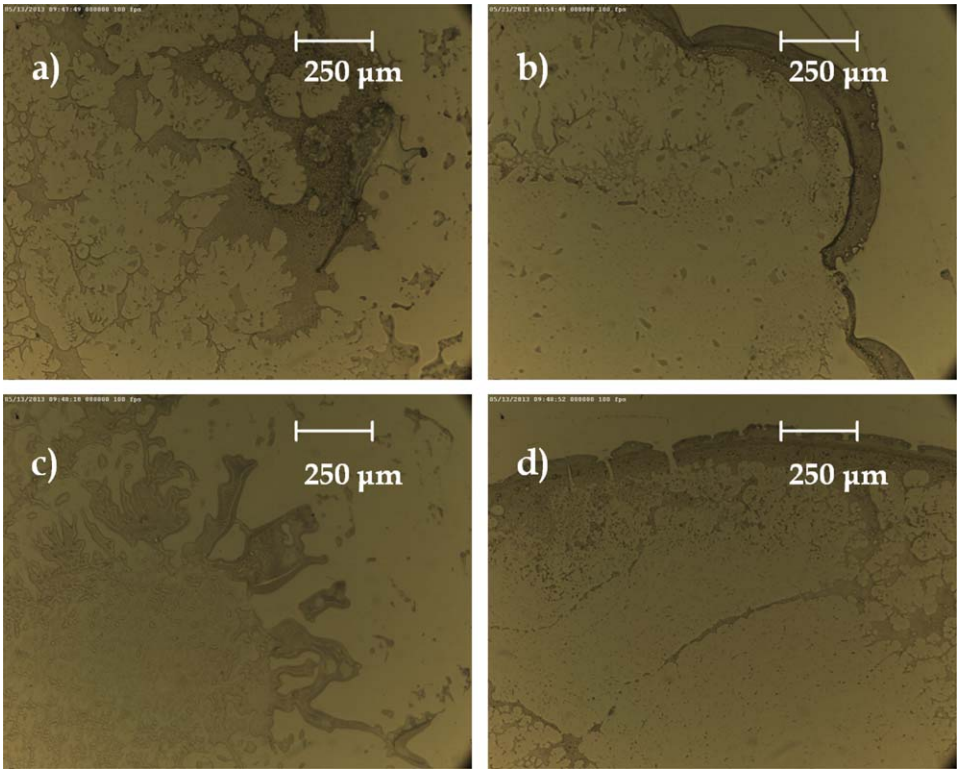

Figure 11. Not a single particle was observed on the photographs taken for experiments where h_{r-r} = 10 mm and carbon foam was used. Panels (a), (b), (c), and (d) show evaporated fractions of effluent for rotational velocities of 41.9, 73.3, 115, and 178 rad s^{-1}, respectively.

[Color figure can be viewed in the online issue, which is available at wileyonlinelibrary.com.]

Image Analysis

The microscopic photographs taken from the dried Petri dish samples were analyzed in MATLAB 2013a using the functions `im2bw` and `imfindcircles`, which are both part of MATLAB's Image Processing Toolbox.

The function `im2bw` is first used to convert the photograph from its original RGB-state (Red, Green, Blue), via an intermediate grayscale stage, to a black and white image. A threshold level is chosen by the user between 0 (black) and 1 (white), below and above which grayscale values are turned into black and white, respectively. The `imfindcircles` function then makes use of a so-called Phase Coding method, where the likelihood of the presence of a circle in the black and white image is estimated using a sensitivity factor. This sensitivity factor can be set to any value in the range between 0 and 1 and corresponds to the tolerance for detecting a circle in the image; the closer this value lies to unity, the more circles will be found at the risk of finding false positives.

To accurately find circular particles in the microscopic images, first an initial pass through these two functions is made. Under this initial run, the sensitivity factor (in `imfindcircles`) and threshold level (in `im2bw`) are slightly adjusted when necessary form their default values 0.85 and 0.225, respectively. An optimal combination of these values

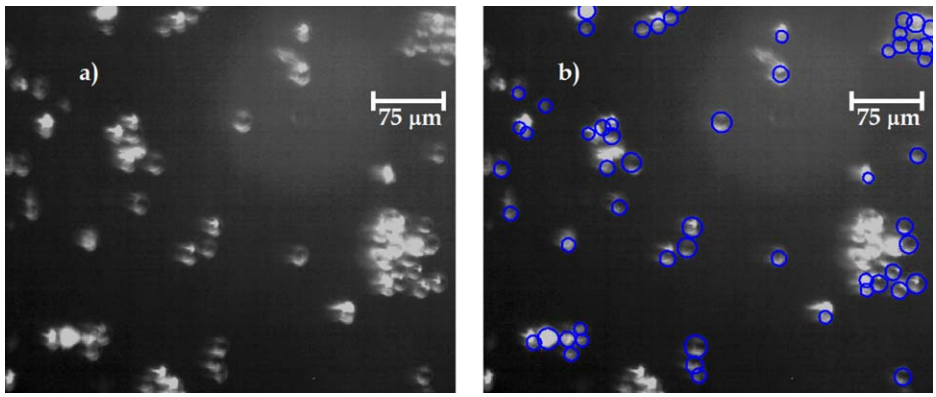

Figure 12. Panel (a) shows a digitally enhanced photograph taken through the microscope for an experiment using the reticulated foam with the smallest particle fraction where d_p is in the range 1–30 µm.

The image analysis algorithm detected particles indicated by the blue circles in (b). The rotational velocity of the rotor-rotor assembly was equal to 52.4 rad s^{-1}. [Color figure can be viewed in the online issue, which is available at wileyonlinelibrary.com.]

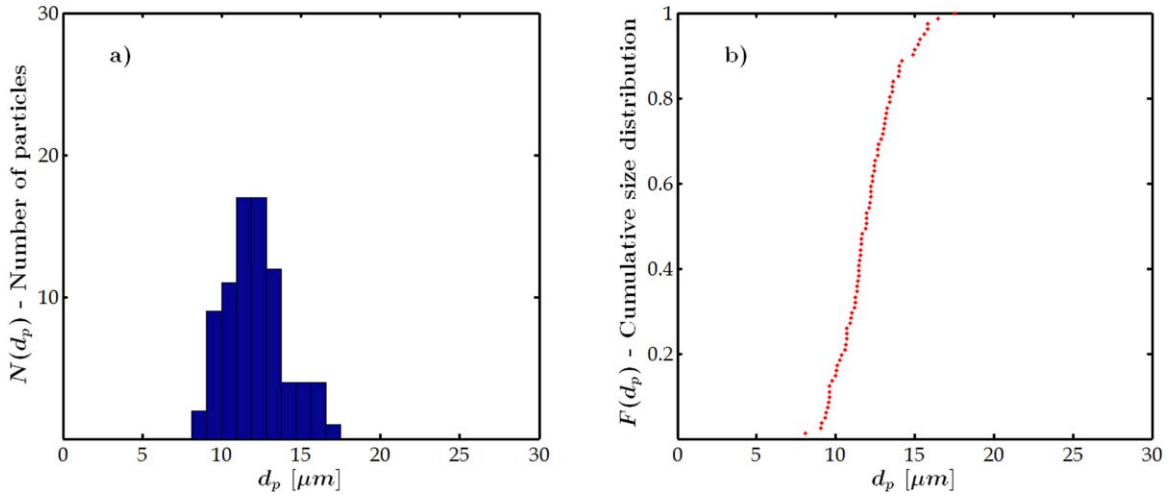

Figure 13. Panel (a) shows a bar plot of the experimental result corresponding to Figure 12, while panel (b) details the corresponding cumulative particle-size distribution.

[Color figure can be viewed in the online issue, which is available at wileyonlinelibrary.com.]

was then found when simultaneously the number of false positives was as low as possible, the number of true positives was as high as possible, and the number of missed particles was again as low as possible. This first step then resulted in the conversion of the original image in panel (a) in Figure 7 to the black and white picture in panel (b). Another factor that was taken into account during this initial phase was the sharpness of fit of the circle's edge over the particle's. When the black-and-white threshold level was not properly set, the found circumferences could be erroneously fitted through the particle's shadow, or inside the particle body. By carefully adjusting both the sensitivity factor and the threshold level, these problems could be circumvented.

After this first step, a number of circles was found as depicted in Figure 7c. These circles were defined by their (x,y)-coordinates in the image, their radii, and a value corresponding with its likeliness of fit from the Phase Coding method. Following visual inspection of this preliminary result, it was possible to manually remove false positives, manually add individual particles by clicking on three points on the edge of the particle, or locally find other particles using other values for the sensitivity factor and threshold level. This last step was particularly useful when the image displayed a gradient in background lighting. The final, resulting image can then be seen in Figure 7d.

The final list of circle positions and radii in pixels was then converted to a list of particle diameters using the magnification factor for the photographs of 1.2 μm px^{-1}. A particle-size distribution for this specific example was plotted as in Figure 8, from which the largest observed particle diameter, the average particle diameter, the standard deviation and 99% confidence interval were obtained.

Results and Discussion

The results of the particle containment experiments pertaining to $h_{r-r} = 1$ mm in the absence of the carbon foam are shown in Figure 9. For this particular situation, particle entrapment is very poor. In fact, particles of all sizes are seen to come out of the reactor. For the case of a large rotor-rotor spacing of $h_{r-r} = 10$ mm without a reticulated foam, particle entrapment is also quite poor as can be seen in Figure 10. Even though the distance between the rotors is one order of magnitude larger, the containment results are qualitatively similar. This is in line with the observations made by Owen and Pincombe[17] and Owen et al.[18] where the Bödewadt boundary layers attached to the rotors act as a focus for the centripetal throughflow, while their thicknesses are independent of the distance between the two disks. So, even though the average radial velocity between the two disks would be 10 times lower when increasing the rotor-rotor spacing from 1 to 10 mm, the average radial velocity inside the boundary layers remains unchanged. This consequently leads to the same poor entrapment results as observed in the experiments where the spacing between the rotors equals 1 mm. Note that less particles were observed in the effluent for the situation where

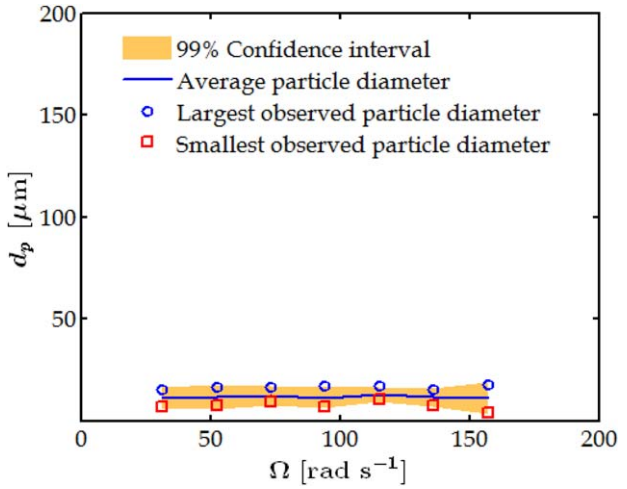

Figure 14. Full containment of glass beads with a particle diameter larger than d_p>17.8 μm is observed in the experiments where the rotor-rotor spacing equals 10 mm, which is filled with a highly porous carbon foam.

The reticulated foam hinders the formation of Bödewadt boundary layers, allowing for better particle entrapment. [Color figure can be viewed in the online issue, which is available at wileyonlinelibrary.com.]

$h_{r-r} = 10$ mm than was the case when $h_{r-r} = 1$ mm. Additionally, no particles where found in the effluent stream for high rotational velocities, that is, $\Omega = 115$ rad s^{-1}. Apparently, the larger rotor-rotor gap spacing leads to a slightly better particle containment, but it is still too unreliable to be useful.

The formation of boundary layers between the disks appears to be hindered, however, when the reticulated carbon foam is installed. As can be seen in Figure 11, all particles in the size ranges 30–50 and 50–80 μm are fully entrapped. Furthermore, as becomes clear from Figures 12–14, the largest observed particle diameter was found to be $d_p^{\max} = 17.8$ μm, for the case where the reticulated foam was used at a rotor-rotor distance of 10 mm and glass beads with a diameter in the range of 1–30 μm. The corresponding value of the cumulative particle-size distribution for this diameter in Figure 4 is equal to $F(d_p^{\max}) = 0.80$. Furthermore, given the fact that on average 79.3 glass beads where identified per photograph, the chance of not observing a particle larger than $d_p^{\max}$ while it would be present in the effluent is calculated to be $P = \left(1 - F(d_P^{\max})\right)^{79.3} = 3.73 \times 10^{-56}$. It is, therefore, nearly certain that glass beads with a size down to 17.8 μm can be fully entrapped in this configuration.

A remarkable observation that can be made from Figure 14 is the constant value of $d_p^{\max}$ when changing the angular velocity of the rotor-rotor assembly. When considering the forces acting on a spherical glass bead that is just entrapped at the edge of the rotor-rotor construction, the centrifugal buoyant force can be written as

$$F_c = \frac{\pi}{6}(d_p^{\max})^3(\rho_P - \rho_L)\Omega^2 R_D \tag{1}$$

where ρ_P and ρ_L are the densities of the particle and the liquid, respectively. The other major force that works on the particle is the drag force acting radially inward

$$F_d = -\frac{\pi}{8}(d_p^{\max})^2 C_D \rho_L v_r^2 \tag{2}$$

where v_r is the velocity difference between the particle and the liquid in the radial direction. The drag coefficient C_D is a function of the Reynolds number

$$Re_p = \frac{\rho_L d_p^{\max} v_r}{\mu_L} \tag{3}$$

where μ_L is the dynamic viscosity of the liquid. When a particle is just entrapped, the net force on it will be zero so that Eqs. 1 and 2 are set to be equal. Rearranging of $F_c = F_d$ yields

$$C_D v_R^2 = \frac{4 d_p^{\max}(\rho_P - \rho_L)\Omega^2 R_D}{3\rho_L} \tag{4}$$

In order for $d_p^{\max}$ to not be a function of Ω, it is thus required that $C_D v_R^2 \propto \Omega^2$. For very low Reynolds numbers (Stokes flow), the drag coefficient can be expressed as

$$C_D = \frac{24}{Re_p} \tag{5}$$

$$C_D = \frac{24\mu_L}{\rho_L d_p^{\max} v_r} \tag{6}$$

while for Reynolds numbers much larger than 1000, C_D is a constant. Therefore, for Stokes flow, one obtains a proportionality where $v_r \propto \Omega^2$, which cannot be described by Bödewadt flow. Obviously, this cannot be satisfied when the radial component of the flow field is fully dominated by throughflow either, as

$$v_r \propto \frac{\phi_v}{2\pi R_D h_{r-r}} \tag{7}$$

For the case of very high Reynolds numbers where C_D is a constant, it must hold that $v_r \propto \Omega$. Although this is in line with the similarity assumption underlying Bödewadt flow, the largest Reynolds number for 17.8 μm particles and an angular velocity of 179 rad s^{-1}, is calculated to be equal to $Re_p = 21$. From this, two conclusions can be drawn. First, it can be concluded that Bödewadt layers are not formed between the interior region between the rotors. Second, a simple force balance based on centrifugal buoyancy and drag is insufficient to explain the constant value for the maximum particle diameter when changing the angular velocity of the rotor-rotor assembly.

Concluding Remarks

A novel configuration of the rotor-stator spinning disk reactor is proposed where the rotating disk is replaced with two conjoined rotating disks with a rotor-rotor spacing of 1 mm, or 10 mm. In addition, the interior domain between the rotors for the 10 mm case could be filled with a highly porous reticulated carbon foam. This configuration allows for the entrapment of spherical glass beads so that the setup can be used for solid-liquid multiphase reactions without needing to catalytically coat the rotating disk, mechanical filtering of the effluent stream, or downstream processing of the product stream to recover the solid fraction.

It was found that particle containment was poor without the use of the porous carbon foam due to the formation of Bödewadt boundary layers attached to the interior of the rotating disks. These boundary layers act as a focus for the net throughflow, increasing the centripetal drag force on the glass beads hampering particle entrapment. The effect of changing the rotor-rotor distance on the magnitude of the drag force is negligible as the Bödewadt boundary layer thickness is not a function of the rotor-rotor spacing, in line with the observations done by Owen and Pincombe[17] and Owen et al.[18]

The addition of a highly porous reticulated carbon foam between the two rotating disks hindered the formation of the Bödewadt boundary layers, improving the confinement of glass beads inside the experimental setup. Particle entrapment for this situation showed good results, where glass beads with diameters down to 17.8 μm could be fully contained inside the reactor. The diameter of the largest particles that were observed in the effluent stream was found to not be a function of the azimuthal velocity of the rotor-rotor assembly. Moreover, a simplified force balance based on centrifugal buoyancy and drag does not seem to be able to account for this effect.

Acknowledgments

The authors gratefully acknowledge the European Research Council (ERC) for their financial support to this project (ERC contract: 227010). In addition, the authors extend their gratitude to Christian Schwarz of the TU Dortmund, Germany, for his experimental contribution to this work.

Literature Cited

1. van der Schaaf J, Visscher F, Bindraban D, Schouten JC. *Device for Multi Phase and Single Phase Contacting*. U.S. Patent Appl. 14/113,903, 2012.

2. van Eeten KMP, Houben HHH, van der Schaaf J, Schouten JC. An experimental and theoretical study on the size of bubbles formed between a rotating disc and a stationary wall. *Chem Eng Sci*. 2014; 109:251–263.
3. Meeuwse M, van der Schaaf J, Kuster BFM, Schouten JC. Gas-liquid mass transfer in a rotor-stator spinning disc reactor. *Chem Eng Sci*. 2010;65:466–471.
4. Meeuwse M, van der Schaaf J, Schouten JC. Multistage rotor-stator spinning disc reactor. *AIChE J*. 2012;58:247–255.
5. van der Schaaf J, Schouten JC. High-gravity and high-shear gas-liquid contactors for the chemical process industry. *Curr Opin Chem Eng*. 2011;1:84–88.
6. van der Schaaf J, Chilekar VP, van Ommen JR, Kuster BFM, Tinge JT, Schouten JC. Effect of particle lyophobicity in slurry bubble columns at elevated pressures. *Chem Eng Sci*. 2007;62:5533–5537.
7. Meeuwse M, Lempers S, van der Schaaf J, Schouten JC. Liquid-solid mass transfer and reaction in a rotor-stator spinning disc reactor. *Ind Eng Chem Res*. 2010;49:10751–10757.
8. von Kármán T. Über laminare und turbulente Reibung. *Z Angew Math Mech*. 1921;1:233–252.
9. Cochran WG. The flow due to a rotating disc. *Math Proc Camb Philos Soc*. 1934;30:365–375.
10. Bödewadt UT. Die Drehströmung über festem Grunde. *Z Angew Math Mech*. 1940;20:241–253.
11. Batchelor GK. Note on a class of solutions of the Navier-Stokes equations representing steady rotationally-symmetric flow. *Q J Mech Appl Math*. 1951;4:29–41.
12. Stewartson K. On the flow between two rotating coaxial disks. *Math Proc Camb Philos Soc*. 1953;49:333–604.
13. Holodniok M, Kubíček M, Hlaváček V. Computation of the flow between two rotating coaxial disks. *J Fluid Mech*. 1977;81:689–699.
14. Holodniok M, Kubíček M, Hlaváček, V. Computation of the flow between two rotating coaxial disks: multiplicity of steady solutions. *J Fluid Mech*. 1981;108:227–240.
15. Daily JW, Nece RE. Chamber dimension effects on induced flow and frictional resistance of enclosed rotating discs. *J Basic Eng*. 1960;82:217–232.
16. Djaoui M, Dyment A, Debuchy R. Heat transfer in a rotor-stator system with a radial inflow. *Eur J Mech B Fluids*. 2001;20:371–398.
17. Owen JM, Pincombe JR. Velocity measurements inside a rotating cylindrical cavity with a radial outflow of fluid. *J Fluid Mech*. 1980; 99:111–127.
18. Owen JM, Pincombe JR, Rogers RH. Source-sink flow inside a rotating cylindrical cavity. *J Fluid Mech*. 1985;155:233–265.
19. van Eeten KMP, van der Schaaf J, van Heijst GJF, Schouten JC. Boundary layer development in the flow field between a rotating and a stationary disk. *Phys Fluids*. 2012;24:033601.

Manuscript received Oct. 12, 2014, and revision received May 6, 2015.